Measurement and Modeling of Angular Spreads of Three-Dimensional Urban Street Radio Channels

Ruonan Zhang, *Member, IEEE*, Xiaofeng Lu, *Member, IEEE*, Jianping Zhao, Lin Cai, *Senior Member, IEEE*, and Jiao Wang

***Abstract*—By utilizing planar antenna arrays, a base station (BS) by the roadside can exploit two-dimensional (2-D) sectorization and beamforming to connect dense pedestrians and vehicles in a street. The azimuth and elevation angular spreads of the street radio channels are critical for the spatial multiplexing performance. In this paper, by utilizing a multiple-input–multiple-output (MIMO) channel sounder equipped with two uniformed planar antenna arrays, the three-dimensional (3-D) multipath propagations in urban macrocellular street canyon environments were measured and modeled, with the focus on the dynamics of the angular spreads along the streets. The transmitter (emulating a user equipment, UE) was placed at 100 and 95 positions in two streets for the line-of-sight (LOS) and non-line-of-sight (NLOS) scenarios, respectively. The azimuth/elevation angle-of-arrival (AoA/EoA) and the root-mean-square azimuth/elevation spread of arrivals (ASA/ESA) at each position were measured. Contrary to the expected monotonous change of the angular spreads with respect to the UE–BS distance, the measurement results show that, in the LOS scenario, ASA and ESA have a positive correlation with the UE–BS distance in an open street but a negative correlation in a closed street. In the NLOS scenario, the correlation is positive when the UE is close to a building without the over-rooftop diffraction, but the correlation is reversed if such a *Quasi-LOS* path exists. The 2-D arrival profiles of the ray clusters have been observed, and their impacts on the angular spreads are analyzed in different propagation environments. By comparing multiple candidate fitting functions, the lognormal distribution models for ASA and ESA are proposed. In addition, the channel delay spread (DS) was also measured along the streets and positive correlations among ASA, ESA, and DS have been found. This work can help to establish the 3-D spatial channel models for advanced MIMO technologies and is also valuable for future channel measurements.**

***Index Terms*—Angular spread, delay spread (DS), microwave measurement, multipath channels, radio propagation.**

I. Introduction

FULL dimensional multiple-input–multiple-output (FD-MIMO) has recently been recognized in the 3GPP community as one of the key next-generation cellular technologies to enhance MIMO systems [1]. By employing planar antenna arrays and active antenna system (AAS) technologies, the additional control over the elevation dimension enables advanced vertical sectorization (e.g., adaptive control over the vertical pattern beamwidth and/or downtilt) and user-specific elevation beamforming. FD-MIMO extends spatial separation to the elevation domain as well as the traditional azimuth domain. A promising application is for a base station (BS) by the roadside to provide connections to dense pedestrians and vehicles along a street with increased signal-to-interference-plus-noise ratio and throughput.

The performance of sectorization and beamforming by FD-MIMO is determined by both AASs and spatial propagation characteristics of radio channels. The angular spread of wireless channels describes the power arrival dispersed over the incident angles, which is caused by the multipath propagation, as illustrated in Fig. 1. The angular spread is an important channel property for spatial transmission systems. For example, in the signal reception by beamforming, if the angular spread at the BS is small, the significant multipath components (MPCs) from a UE are more concentrated to the most significant path and the power spraying into adjacent beams will be small, leading to a low intersector interference. Thus, better spatial multiplexing performance may be possible, and vice versa. Therefore, characterizing the three-dimensional (3-D) propagation directions and angular spreads in both the azimuth and elevation dimensions is critical to exploit the antenna array and MIMO technologies.

In recent years, the 3-D channel characterization and modeling have drawn great interest in both the industrial and academia communities. The traditional two-dimensional (2-D) channel models assume a zero elevation angle of each signal path, such as the 3GPP spatial channel model (SCM) [2]. In extending the traditional models into 3-D, the WINNER II [3], WINNER+ [4], COST2100 [5], and 3GPP [6] have proposed the 3-D geometric stochastic SCMs which associate true elevation angles with

Manuscript received April 22, 2015; revised January 25, 2016; accepted August 2, 2016. Date of publication August 30, 2016; date of current version May 12, 2017. This work was supported in part by the NSERC, in part by the NSFC under Grant 61571370, Grant 61301092, and Grant 61601365, in part by the Natural Science Basic Research Plan in Shaanxi Province under Grant 2015JM6349 and Grant 2016JQ6017, and in part by the National Civil Aircraft Major Project of China under Grant MIZ-2015-F-009. The review of this paper was coordinated by Prof. C. P. Oestges. The preliminary results of the channel measurements in this paper have been presented in part at the IEEE International Conference on Communications 2014 Sydney, NSW, Australia. The new contributions of the journal submission include the literature review in Section II, more detailed description on the channel measurement approach in Section III, typical power arrival profiles and propagation mechanism analysis in Section V, modeling of the angular spreads in Section VII, and measurement results of the channel delay spread and correlations between the angular spreads and delay spread in Section VIII.

R. Zhang and J. Wang are with the Department of Communications Engineering, Northwestern Polytechnical University, Xi'an 710072, China (e-mail: rzhang@nwpu.edu.cn; jwang@mail.nwpu.edu.cn).

X. Lu and J. Zhao are with Huawei Technologies Ltd., Shanghai 200127, China (e-mail: stan.lu@huawei.com; peter.zhao@huawei.com).

L. Cai is with the Department of Electrical and Computer Engineering, University of Victoria, Victoria, BC V8P 5C2, Canada (e-mail: cai@ece.uvic.ca).

Color versions of one or more of the figures in this paper are available online at http://ieeexplore.ieee.org.

Digital Object Identifier 10.1109/TVT.2016.2604394

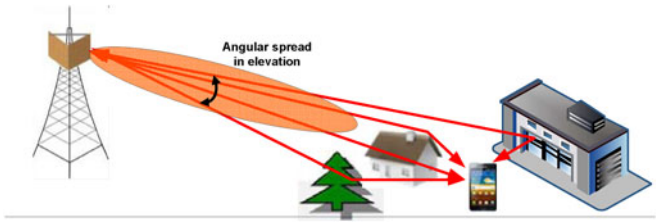

Fig. 1. Illustration of vertical beamforming and angular spread in elevation.

signal paths. In addition to the large-scale spatial parameters in the 2-D channel models, *root-mean-square (RMS) azimuth spread of arrival/departure (ASA/ASD)*, two new elevation-related parameters, *rms elevation spread of arrival/departure (ESA/ESD)*, are defined. Their distributions and correlations with other fading parameters, such as path loss and delay spread (DS), are characterized for typical cellular scenarios. These models have provided useful tools for the simulation and performance evaluation of the emerging advanced 3-D beamforming and spatial multiplexing technologies. However, the dynamics of the angular spreads for a mobile UE have been less explored, and the effect of surrounding environments on their variation needs more in-depth investigation. For example, in the radio vehicle-to-infrastructure access networks, how do ASA and ESA vary when a vehicle is moving along a street? How do the roadside building layouts affect the angular spread and fading of the MPCs? For future high density and mobile access in urban streets, studying the dynamics of the channel characteristics along a street and modeling the spatial street channels are needed.

In this paper, the ASA, ESA, and DS of the urban macrocellular (UMa) channels in two typical street canyon environments for the line-of-sight (LOS) and non-line-of-sight (NLOS) scenarios are investigated by extensive field measurements and modeling. The main contributions of this paper are as follows.

First, a measurement campaign for the radio channels in typical urban streets was carried out by the joint effort of the Northwestern Polytechnical University (NPU) and Huawei Technologies Ltd. The receiver (Rx, emulating a BS) was installed on the rooftop of a five-storey building and the transmitter (Tx, emulating a UE) moved on the rectangular grids along two streets for the LOS and NLOS scenarios. The 3-D propagations were measured using two uniformed planar antenna arrays (UPAs), each containing two dual-polarized 4×4 dipole matrices. A direct-sequence spread spectrum (DSSS) transmission scheme was employed to probe the channels with the bandwidth of 62.5 MHz and carrier frequency of 2.6 GHz. The uplink LOS channels were measured with the UE located at 100 positions in a street and the NLOS channels were measured with the UE at 95 positions on another street. At each UE position, the incident angles of each individual propagation path, including the *azimuth angle of arrival (AoA)* and the *elevation angle of arrival (EoA)*, were jointly estimated based on the captured array signals on the receive UPA. Then, the 2-D power arrival profiles and ASA/ESA of the MPCs impinging to the BS were obtained.

Second, the variations of ASA, ESA, and DS when the UE moved along the streets were observed and interesting results have been found. Different from the anticipated monotonic change with respect to the UE–BS distance, their values fluctuated when the UE moved toward or away from the BS. In an open street without buildings by the roadsides, ASA and ESA increased when the UE–BS distance increased, and vice versa. But the trend was reversed in a closed street where buildings existed on one or both roadsides, i.e., the angular spreads decreased with the increase of the UE–BS distance. By analyzing the observed multipath power arrival profiles in the azimuth–elevation plane, the impact by the roadside building layout on the ASA and ESA in the LOS scenario is revealed. For the NLOS scenario, the over-rooftop diffraction (*Quasi-LOS* path) is observed and its effect on the angular spread is also analyzed. When the *Quasi-LOS* path existed, ASA and ESA decreased when the UE was moved further away from the BS. But this trend was reversed without the *Quasi-LOS* path (when the UE was too close to the blocking building).

Third, by comparing several candidate probability density functions (pdfs) in fitting the measured empirical distributions, the lognormal models are proposed for the ASA and ESA distributions. The model parameters are formulated with respect to the UE–BS distance and street environment. The 3-D channel realizations can be generated using the proposed models stochastically.

Fourth, the correlation coefficients among the ASA, ESA, and DS are obtained based on the measurement results. It is found that they have positive correlations with each other in the measured street canyon environments.

This work provides an in-depth insight into the dynamics of the 3-D urban street channels. The measurement results and proposed distribution and correlation models of the angular spreads provide a tool that enables the simulation and performance evaluations for the FD-MIMO to connect dense UEs in a urban street. For example, the power reception and intersector interference in the beamforming and spatial multiplexing can be analyzed. This work also provides a valuable reference for future channel measurement campaigns.

The rest of the paper is organized as follows. Section II overviews the related industry standards and literatures on 3-D channel modeling. Section III introduces the design and verification of our MIMO channel sounder. The measurement setup in the LOS and NLOS scenarios is described in Section IV. In Section V, the measured 2-D spatial power arrival profiles from four UE positions in various propagation environments are presented, and the propagation mechanisms are analyzed. The variations of ASA and ESA with respect to the UE–BS distance and the impact by the roadside building layout are evaluated in Section VI. The statistical models of the angular spreads are proposed in Section VII. Section VIII presents the measurement results of DS and the cross correlations among the angular spreads and the DS. The limits in this measurement campaign and the solutions are discussed in Section IX. Section X concludes the paper and points out future research issues.

II. Related Work

A. 3-D Channel Model Standards

3-D channel modeling enables radio propagation characterization in both the elevation and azimuth domains. Inspired by the attractive features and potential benefit of FD-MIMO, several standardization projects, such as the WINNER, COST, and 3GPP, have made significant achievements in defining the full 3-D bidirectional, dual-polarized MIMO channels. These channel models have provided useful tools for the design and performance evaluation.

The 3-D MIMO channel model, SCM-enhanced, defined in WINNER II [3] and WINNER+ [4] have been evolved from the WINNER I channel models. The novel features include the elevation parameterization for selected scenarios and the scenario-dependent polarization modeling. The elevation angles of paths are drawn by following the same approach as the azimuth angles, and the original ASA and clusterwise ASA values are replaced by the corresponding elevation parameters. Due to the limit of measurement results on the new large-scale parameters, a cross-correlation coefficient is set to zero if the measured value is less than 0.4 or values for other scenarios if unavailable.

3GPP has also paved the way to full 3-D channel modeling. 3GPP initialized a study item in 2012 [7] and the latest technical report (TR 36.873) [6] was released in June 2015. The new scenarios for UE-specific elevation beamforming, such as the UMa cell with high outdoor/indoor UE density, are specified for the application of 3-D channel models. In both the WINNER and 3GPP models, azimuth power spectra (APSs) of clusters are modeled as the wrapped Gaussian function. The AoAs and azimuth angle of departures (AoDs) of paths are generated by applying the inverse Gaussian function with the cluster power and ASA given for specific scenarios. On the other hand, the cluster elevation power spectra (EPSs) are Laplacian distributed. Then the EoAs and elevation angle of departures (EoDs) are determined by applying the inverse Laplacian function, given the cluster power and angular spreads.

The European Cooperation in Science and Technology (COST) project has delivered the COST2100 channel model [5], which characterizes the 3-D channels at the individual-cluster level. A cluster is depicted as an ellipsoid in space with its size being determined by the axes along different directions. It is proposed that cluster angular spreads in both the azimuth and elevation planes follow the lognormal distribution with a base of 10. Based on the field measurements, the cross-correlation coefficient between DS and ESA is 0.5 for both the LOS and NLOS indoor scenarios.

B. Research on 3-D Spatial Channel Modeling

In recent years, significant efforts have been exerted to study the elevation-domain propagation characteristics by field measurements and numerical simulations. The measurements in different environments in [8] have shown that the power arrival in elevation plane has a double-sided exponential distribution with different slopes on the negative and positive sides of the peak in the NLOS situation. The authors in [9] investigated signal power distribution in AoA, EoA, and time-of-arrival (ToA) domains for various positions in an array of buildings along a grid of straight streets. But the impact of the roadside building layout on the angular spreads was not analyzed. The distribution of EoA, extracted from measurements, has been reported in [10]. The results showed that MPC clusters were usually generated by the building walls, roof edges, or trees, which had LOS paths to both the BS and the UE. The description of EoA was included in the 3-D fading channel model in [11], where an elevation offset angle was introduced and modeled by a distance-dependent exponential function. The EoA and ESA properties were studied analytically in [12] using the ray-tracing method. The authors selected two U.K. cities of Bristol and London. The elevation-dimension propagations in both the pico- and macroscenarios were generated numerically. It was shown that the ESA depended strongly on the UE–BS distance, as it changed from a mean of 5° when the UE was close to the BS to around 0.3° with the distance of more than 600 m. It was also observed that the variance of ESA decreased with distance.

The measurement and modeling of 3-D channels have also appeared recently and several research groups have done important works. The multidimensional propagation measurement data in urban micro- and macrocellular environments were compared with the analytical results by 3-D ray tracing in [13]. It was shown that the diffuse scattering had a significant impact on urban propagation characteristics and accurate environment representation was critical on the model prediction. An extensive channel sounding campaign was performed in an urban macrocell in Cologne, Germany, using a MEDAV RUSK MIMO channel sounder [14]. The fixed Tx was mounted on a rooftop approximately 30 m high and the mobile Rx was set up in a car. By adopting dual-polarized, circular antenna arrays on both link ends, the full 3-D channels were measured at 2.53 GHz. The measurement data were evaluated by the high-resolution parameter estimation framework, RIMAX. It could not only remove the effect of antennas to obtain independent channel characterization but also achieve high accuracy and fidelity by modeling a channel as the superposition of a deterministic (specular) and a stochastic (dense multipath) part. The AoA/EoA, AoD/EoD, and complex polarimetric path weights were estimated and then the RMS parameter spreads were derived.

Prof. Narandzi's group has made significant efforts and contributions on the implementation and experiments of 3-D channel modeling. The measurements for the UMa scenario in two German cities in [15] verified the WINNER model and, in particular, empirically revealed the variation of the measurement results. Links from three different BSs toward seven mobile tracks were sequentially monitored. The BS (Tx) array was placed 3–4 m above the building rooftops. The mobile terminal antenna array was mounted on top of a car at approximately 2 m above ground and moved by a moderate speed of 3–5 m/s. The measurements were performed using a RUSK channel sounder operating at 2.53 GHz with a bandwidth of 100 MHz. In [16], the authors approximated the WINNER scenarios with multivariate normal distributions and then quantified the mean Kullback–Leibler divergence. The results showed that the WINNER scenario groups (A, B, C, and D) or propagation classes (LOS, obstructed LOS (OLOS), and NLOS) did not necessarily ensure minimum separation within the groups/classes. Then, a grouping method that minimized intragroup distances was proposed.

In [17], the stationarity of the outdoor environment between repeated measurements was evaluated. In the authors' measurements, the BS was fixed and the mobile receiver moves twice over the same track. By comparing the large-scale parameters derived from the two measurements, it was found that a multirun repeated measurement procedure causes a low decorrelation of estimated delay and azimuth spreads. The observation indicated that large-scale characterization of a multilink configuration could be performed by consecutive measurement runs using a single sounding device.

For the channel simulation, under the framework of SCM in WINNER, the authors showed that the analysis of antenna translation and rotation effects could be separated based on the plane wave assumption [18]. When a rotation of 3-D antenna beam patterns was performed in the preprocessing phase, the complexity of channel simulations could be reduced, but the reduction of the total complexity depended on the representation complexity of the patterns and the number of MPCs used in simulations.

Prof. Zhang's group from Beijing University of Posts and Telecommunications has conducted a series of 3-D channel measurements by using the EB PropSound, a wideband multiantenna radio channel sounder at a carrier frequency of 3.5 GHz and with a signal bandwidth of 100 MHz. The channel parameters were extracted by the spatial-alternating generalized expectation-maximization algorithm. In [19], 3-D MIMO measurements were conducted in China (3.5 GHz) and New Zealand (2.35 GHz) for the outdoor-to-indoor (O2I) UMa environment. The 16×16 3-D MIMO channel impulse response (CIR) was reconstructed, and the channel capacity was predicted from the measured data for different antenna array topologies. In [20], a measurement campaign was carried out to parameterize the clusters in O2I channels. By employing an automatic clustering algorithm on the multipath channel responses, clusters were identified jointly by the AoA, AoD, EoA, EoD, and delay. The intra and intercluster statistical properties were analyzed. The 3-D MIMO channel in the typical UMa scenario was measured in both the temporal and spatial domains in [21], and a distance-dependent ESA model was proposed. The results showed that the distribution of EPS could be modeled by the Laplacian pdf and Gaussian pdf for the LOS and NLOS channels, respectively, while the distributions of ESA and ESD could be modeled by the lognormal pdf. Furthermore, ESA decreased with the increase of transceiver distance in the LOS scenario due to the ground reflection rays.

In 2013, the research group in Huawei performed measurements on EoA and EoD in the urban macrocell (UMa) and urban microcell (UMi) scenarios in Xi'an, China [22]. The ESA and ESD and their cross-correlation coefficients with other large-scale channel parameters were calculated and compared with the 3-D ITU IMT-advanced channel models. Based on the measurement results, modifications were proposed for the conventional settings of the LOS-path polarization matrix defined in the WINNER+/ITU/3GPP SCMs.

In our recent field channel measurement campaigns, the 3-D indoor-to-outdoor uplink channels with UE located from the first to fourth floors were measured for the UMa and UMi scenarios in [23] and [24]. The results showed that the distributions of EoA and ESA could be well modeled by the Laplacian and lognormal pdfs, respectively. Moreover, in the UMi scenario, ESA decreased slowly when the UE was located higher inside a building, but it had no clear tendency with the change of UE height in the UMa scenario. We have also performed measurements of the indoor 3-D channels [25], where the distributions of EoA and ESA in the typical hall and corridor environments were obtained.

C. New Contributions in This Study

The above-mentioned works have provided not only key insights into the spatial propagation characteristics of 3-D radio channels but also inspiration for the channel measurement methodologies. The obtained distributions and cross correlations of the arrival/departure directions and angular spreads of the MPCs have supported the extension of the traditional 2-D channel models into 3-D, as reviewed in Section II-A.

The work in this paper aims to further parameterize 3-D wireless channels, with the focus on the dynamics of ASA, ESA, and DS along urban streets [26]. The variations, distributions, and cross correlations of the angular and temporal spreads are studied for both the LOS and NLOS scenarios in typical urban streets. Furthermore, the impact by the roadside building layout on the channel characteristics is revealed based on the measured 2-D spatial power arrival profiles.

In addition, the spatial multipath propagation on the BS side is characterized in this work. This is significant because, first, planar antenna arrays will be mounted on BSs to exploit the spatial property of radio channels (e.g., spatial multiplexing). Second, in practical cellular systems, the advanced complicated algorithms, such as beamforming, precoding/process, and channel state estimation, should be performed by BSs. In particular, the results are useful for the elevation beamforming and FD-MIMO for radio access of dense UEs in urban streets. The limits on the channel sounder capacity and measurement scenarios in this work, as well as the future works, will be discussed in Section IX.

III. Measurement System and Verification

A. Measurement System

The MIMO channel sounder was developed by Huawei and NPU, as shown in Fig. 2, to perform the 3-D propagation measurements. The Tx and Rx systems were placed in two movable cabinets. Two dual-polarized UPAs were mounted on top of the cabinets, and their centers were at the height of 2.1 m above the ground. One UPA was composed of 16 pairs of crossed patches that were organized in a 4×4 matrix. Adjacent patches were spaced by half a wavelength [see Fig. 2(c)]. Each pair included two dipoles with $\pm 45^\circ$ polarizations. Thus, a UPA had 32 dipoles that formed two 4×4 antenna arrays with cross polarizations. One dipole had 7 dBi gain and $-70^\circ \sim +70^\circ$ -3 dB angular width on both the horizontal and vertical planes.

The platform was a DSSS system. A pseudonoise (PN) sequence with the length of 1023 chips and a bit rate of 62.5 Mb/s was generated repeatedly as the baseband signal, leading to a spreading gain of 30 dB. Five of the PN-sequence plus a header and a tail form a frame with the duration of 0.1 ms. The frames

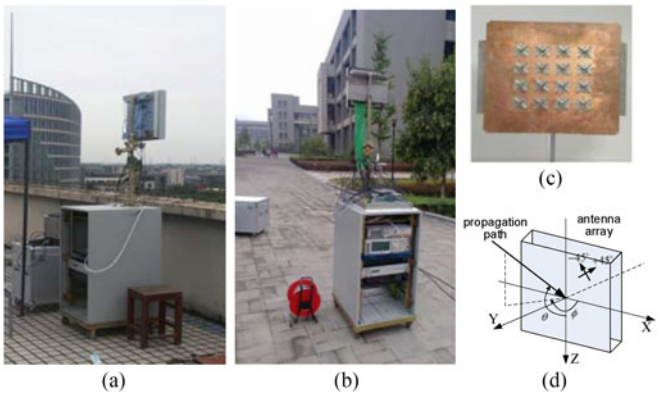

Fig. 2. MIMO channel sounder used in this measurement campaign. (a) Receiver. (b) Transmitter. (c) Antenna array. (d) Coordinate.

were BPSK modulated on the carrier of 2.6 GHz and transmitted over the air.

On the Tx side, a microwave switch with one input and 32 output ports was connected to the 32 dipoles in the UPA. The switch connected one dipole to the signal source and transmitted for 1 ms and then switched to the next dipole. During the 1 ms for each dipole, ten frames of the PN-sequences as mentioned above were sent. On the Rx side, a microwave switch with 32 input and 4 output ports was connected to the UPA that selected the 4 dipoles in one column and output the received signal to the low noise amplifiers and bandpass filters. Then the signals were input into the four ports of a Tex70608 oscilloscope where they were sampled by the rate of 625 MHz and stored for offline processing. When one of the Tx dipoles was transmitting, the switch on the Rx connected the four dipoles in one column (in one polarization) for 0.1 ms to receive a complete frame. Then the switch selected the four dipoles in the next column (in the other polarization), and so on. Thus, it took $8 \times 0.1 = 0.8$ ms to connect all the 8 columns (32 dipoles) of the Rx UPA to receive the sounding signal. As mentioned above, one dipole of the Tx UPA transmitted for 1 ms. Thus, while one Tx dipole was transmitting, each of the 32 dipoles on the Rx UPA received a complete frame of the sounding signal. The waveforms on the 32 Rx dipoles formed a signal set, which was a *spatial channel snapshot*. Two GPS-triggered rubidium clocks provided synchronized clocks to the Tx and Rx to trigger the signal generation and capture and the switch of the antenna elements.

In the field measurements, the transceivers were stationary and there were no fast moving objects in the surrounding environments. Hence, the channel could be regarded static during 0.8 ms when the signal set of one channel snapshot was captured. In this work, to characterize the copolarized 3-D propagation, the four dipoles in +45° polarization in the first row and the four dipoles in +45° polarization in the second column were selected to form an "L" shaped antenna array. The waveforms received on this array in each channel snapshot were utilized to estimate the 2-D angle-of-arrival and power of the incoming paths. Suppose that L paths were resolved from the waveforms of a snapshot. Since each path had an AoA and an EoA, the L paths provided L samples of AoA and EoA. Further, according to (2) given in Section III-B, the AoAs and power of the L paths provided one sample of ASA. Similarly, the EoAs and power of the L paths led to one sample of ESA. Therefore, from one snapshot, we obtained one sample of ASA and ESA.[1]

In this measurement campaign, to get the statistics of ASA and ESA, a number of channel snapshots were captured to collect parameter samples when the Tx was placed at one position. The process by which all 32 dipoles in the Tx UPA were transmitted one by one was called a *cycle*. In one cycle, the channel was sounded by 16 times in one polarization and thus 16 independent channel snapshots were captured. At each UE position, the Tx UPA transmitted for ten cycles, generating a total of $16 \times 10 = 160$ snapshots in one polarization. Please note that after one transmitting cycle, the oscilloscope needed about 15–20 s to store the captured waveforms on the hard disk. Thus, it took about 3 min to collect all 160 snapshots.

There was a variation among the 160 snapshots for one Tx position because the movements of people, vehicles, and trees (due to wind) could introduce change of the propagation directions and power of some paths. The variation among the channel snapshots is referred to as the *small-scale spatial fading*. Thus, the collected parameter samples at one Tx position reflect the statistics of the small-scale fading of the channels.

In this work, the power arrival profiles were measured for the MPCs impinging from the front of the BS, i.e., in the angular range of $[0°,\ 180°]$ in both the azimuth and elevation dimensions, because the channels were modeled for the purpose of evaluating the directional transmission/reception by beamforming (e.g., realized by FD-MIMO) or directional antennas on a BS. In practical systems, the main lobe of the antenna pattern should point to the target UEs and mainly receive the signals incoming from the front. The MPCs from the back are suppressed and negligible due to the directional antenna patterns.

B. Signal Model and Data Processing

With the object of describing the 2-D power arrival of significant MPCs, we employ a statistical baseband channel model that incorporates the ToA, AoA, and EoA information. Suppose that there are L specular multipath waves impinging at the Rx. There are M elements in the array and the CIR on the mth element for $m = 0, 1, 2, \ldots, M-1$ is written as

$$h_m(\tau, \phi, \theta) = \sum_{l=0}^{L-1} \alpha_l e^{j\psi_l} s_m(\varphi_l, \vartheta_l)\, \delta(\tau - \tau_l, \phi - \varphi_l, \theta - \vartheta_l) \tag{1}$$

where $\alpha_l e^{j\psi_l}$, τ_l, φ_l, and ϑ_l are the complex gain, excess delay, AoA, and EoA of the lth path, respectively. The total power of the MPCs is normalized by setting $\sum_{l=0}^{L-1} |\alpha_l|^2 = 1$. $s_m(\varphi_l, \vartheta_l)$ is the complex steering factor of the mth antenna for a signal

[1]In the WINNER [3], [4] and other channel models, the Tx is usually used as a BS and the Rx as a UE. Thus, the angular spreads at BS are evaluated as ASD/ESD and those at UE as ASA/ESA. In this work, because the uplink channels were measured where the Rx was BS and the Tx was UE, the ASA/ESA refer to the power angular spreads of the MPCs arriving at the BS. When the carrier frequency does not change, the angular spreads in the uplink and downlink are equivalent due to the channel reciprocity.

impinging at the angle of (φ_l, ϑ_l). It indicates the power attenuation and phase difference of the signal with respect to the reference point. The phase difference includes the phase shift caused by the complex antenna response and also that due to the propagation distance difference. The latter depends on the incident angle and the position of the mth element. Without loss of generality, we take the position of the first antenna element as the reference point.

The algorithms for path identification and parameter estimation are briefly introduced as follows. The signal received on each Rx antenna element was the superposition of the sounding signals propagated through different paths. The path identification, power estimation, and angle-of-arrival estimation were performed in an iterative process. By performing the sliding correlation, the complex impulse responses of paths on the Rx array were extracted from the captured array signals. Then based on the array impulse responses, the 2-D incident angles (EoA and AoA) of paths were estimated using a subspace-decomposition method. Furthermore, because the paths that arrived within one chip could not be separated in the time domain, the spatial smoothing was applied to separate the paths and estimate their incident angles. See [27] for a detailed explanation of the path extraction and parameterization method.

The steering vectors composed of $s_m(\phi, \theta)$ $(m = 0, 1, 2, \ldots, M-1)$ were measured in an anechoic chamber, where ϕ and θ were scanned from 0 to $+\pi$ with the angular interval of 1°. The steering vectors were used in the 2-D angle-of-arrival estimation algorithm [27]. Thus, the effect of the Rx antenna array was removed and antenna-independent channel characteristics could be obtained. In addition, the Rx system calibration was performed at the beginning and the end of each measurement day, and the complex responses of the radio equipments were measured and removed from the captured array signals.

Based on the measured AoA, EoA, and power of the MPCs, the ESA and ASA can be calculated. They represent the spatial power spread of the MPCs with respect to the median angle of arrival. The ESA, denoted by S_E, is defined as

$$S_E = \sqrt{\frac{\sum_{l=0}^{L-1} (\vartheta_l - \mu_{\mathrm{EPS}})^2 \alpha_l^2}{\sum_{l=0}^{L-1} \alpha_l^2}} \tag{2}$$

where μ_{EPS} is the mean of EPS and calculated by

$$\mu_{\mathrm{EPS}} = \frac{\sum_{l=0}^{L-1} \vartheta_l \alpha_l^2}{\sum_{l=0}^{L-1} \alpha_l^2}. \tag{3}$$

The ASA, denoted by S_A, is defined similarly by replacing ϑ_k by φ_k in (2) and (3).

The DS, denoted by S_D, is defined as

$$S_D = \sqrt{\frac{\sum_{l=0}^{L-1} (\tau_l - \mu_\tau)^2 \alpha_l^2}{\sum_{l=0}^{L-1} \alpha_l^2}} \tag{4}$$

where μ_τ is the mean of excess delay and calculated by

$$\mu_\tau = \frac{\sum_{l=0}^{L-1} \tau_l \alpha_l^2}{\sum_{l=0}^{L-1} \alpha_l^2}. \tag{5}$$

IV. Measurement Scenarios

The measurements were conducted on the campus of NPU in the Xi'an city. We selected two streets for the LOS and NLOS scenarios that could be classified as the typical UMa street canyon environments, as specified in the 3GPP standard [2]. The Rx was installed on the rooftop of the School of Electronics and Information (SEI), a five-storey office building, to emulate a BS, as shown in Fig. 2(a). The center of the UPA panel was 24.5 m high and 2.1 m above the surrounding buildings in the measurement area. The panel was 0.5 m away from the edge of the roof. The Tx emulated a UE and was placed at different locations on the streets, as shown in Fig. 2(b).

A. LOS Scenario

The satellite picture and map of the street area are depicted in Fig. 3. The surrounding buildings were all five-storey modern office buildings. The Tx was moved on a rectangular grid along the street, as illustrated in Fig. 3(b). Five UE positions were arranged on a line at a given distance to the BS and a total of 100 positions were measured on 20 lines with the UE–BS distance increasing from 121 m to 406 m. The distances $(D_1,\ D_2,\ \ldots,\ D_{20})$ are annotated in Fig. 3(b).

At each Tx position, the 32 antenna elements on the UPA transmitted one by one for 10 cycles. Thus, for +45° polarization, the Rx UPA collected $16 \times 10 = 160$ channel snapshots (i.e., samples of array signals) at different time instances. Further, from the five measured positions on one line, a total of $160 \times 5 = 800$ snapshots were obtained for a given UE–BS distance. Based on the array signals, the incident angles and 2-D power profiles of the MPCs (the distributions of the power arrival in the azimuth–elevation plane) were estimated.

B. NLOS Scenario

The picture and map of the NLOS measurement area are shown in Fig. 4. The Rx was installed on the rooftop of the SEI building, and the Tx was moved on another street with LOS propagation obstructed by the east wing of the building. The Tx was also moved on a rectangular grid along the street and a total of 95 positions were measured, as illustrated in Fig. 4(b). The measurement method was the same as in the LOS scenario.

V. Illustrative Examples of Propagations in Typical Environments

The measurement results for four UE positions are presented in this section as illustrative examples of the typical propagation mechanisms in the LOS and NLOS street canyon environments. The received power profiles are plotted in the azimuth–elevation planes to demonstrate the 2-D angle-of-arrival and the power of the MPCs.

A. LOS Scenario

In the LOS scenario, we select two UE positions with the UE–BS distances of D_2 and D_7, denoted by UE1 and UE2, respectively. The two positions are circled in Fig. 3(b). We can see that the street is narrow at the UE1 position but becomes

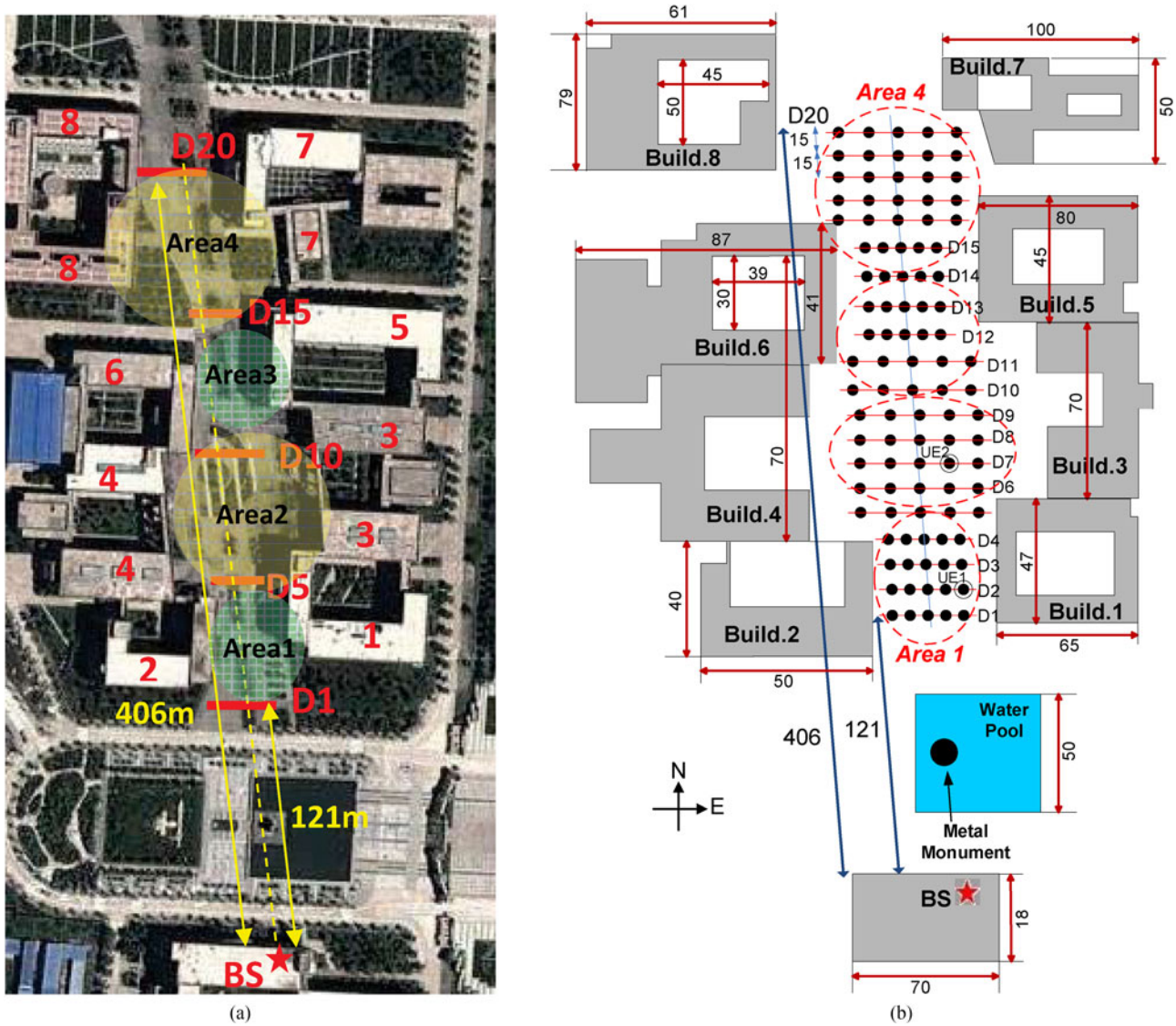

Fig. 3. Street map of the UMa LOS Scenario and Tx positions. The gap between Building 1 and 2 is 40 m; the gap between Buildings 3 and 4 is 75 m; the gap between Buildings 5 and 6 is 35 m; and the gap between Buildings 7 and 8 is 75 m. (a) Measurement area. (b) UE positions on the street (distance unit: meter).

much wider at the UE2 position. Figs. 5 and 6 plot the received power profiles at the BS for the two UE positions. The color bars in the figures are the normalized power (in dB) with respect to the maximum value.

We can see intensive clustered MPCs in Fig. 5(a) for the UE1 position. The spatial power profile is analyzed as follows.

1) The MPC with the largest power (red color) arrived at the EoA of about 79° and AoA about 90°. The PMC can be identified as the LOS path, as it had the strongest propagation and was received from the UE direction.
2) The two clusters on both sides of the LOS path should be the MPCs reflected from Building 1 (School of Power and Energy) and Building 2 (School of Management) located on the two sides of the UE (see Fig. 3). The EoAs of the two clusters concentrated around 83°. Since the waveforms were reflected on the walls of the two five-storey buildings, their EoA should be larger than that of the LOS path that was from the UE on the ground.
3) The cluster slightly below the LOS path in Fig. 5(a) should be the reflection from the ground. Due to the geometry relationship of the UE and BS, the reflection point on the ground should be close to the UE. Therefore, the EoAs of the ground reflection MPCs were slightly smaller than that of the LOS path.
4) The cluster scattered by the metal monument in front of SEI can also be observed. The EoA of this cluster was smaller than that of the ground reflection because the monument was horizontally closer to the BS.
5) The lowest cluster may be scattering from the surface of the large water pool in front of SEI.

The estimated propagation clusters are superimposed on the street photo taken from the BS antenna in Fig. 5(b) (the camera was placed at the center of the BS UPA panel).

The second example is for the UE2 position in a wider street, as shown in Fig. 6. We can see that the MPC with the largest power arrived through the LOS path at the EoA of about 82°,

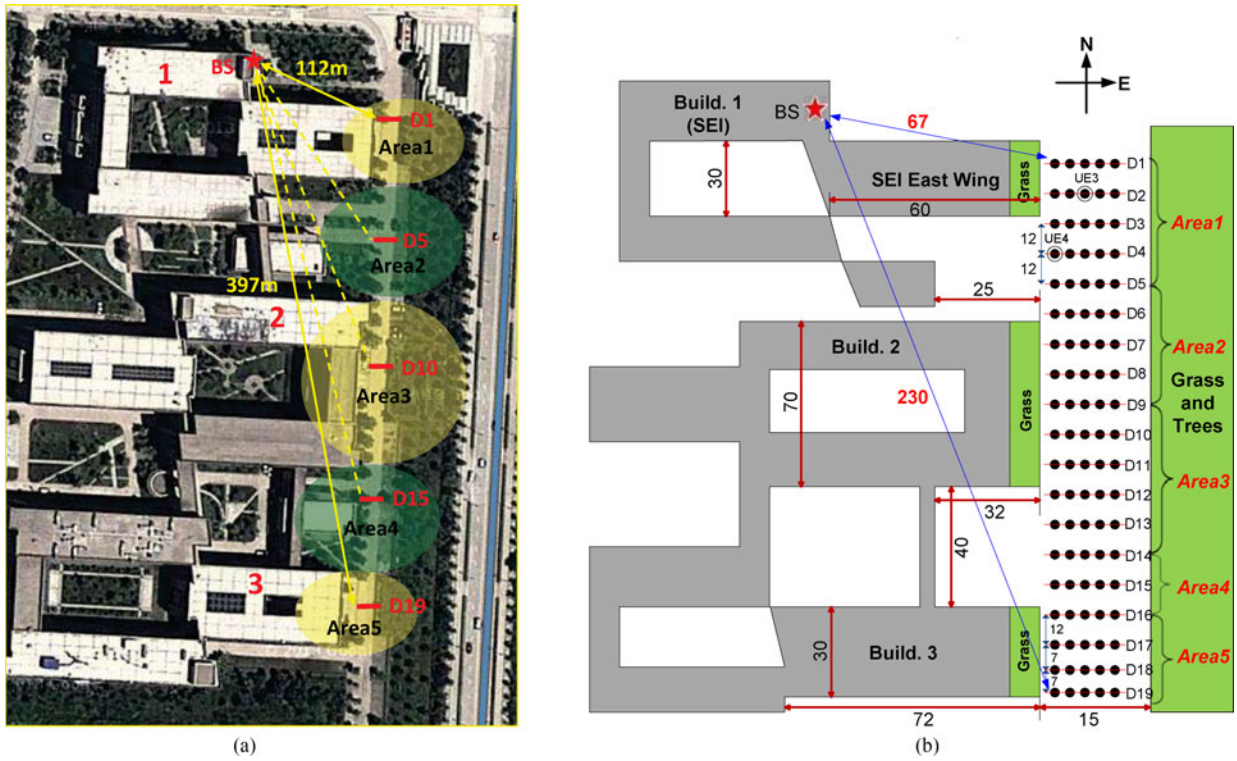

Fig. 4. Street map of the UMa NLOS scenario and UE positions. (a) Measurement area. (b) UE positions on the street (distance unit: meter).

similar to the UE1 case. The clusters reflected from Buildings 1 and 2 can also be observed. However, because the UE was further away, the EoAs of the reflected paths on the two buildings were closer to the LOS path, as observed in Fig. 6(a). The elevation rays caused by ground reflection can still be found whose EoAs were slightly smaller than that of the LOS path. Similarly, the cluster scattered from the metal monument can also be seen, and its EoA was still smaller than that of the ground reflection. However, the scattering from the pool cannot be observed. This may be because the position of UE2 was quite far away from the pool, such that the waveforms from the UE antenna were almost parallel to the surface of the water. Thus, the reflection by the water surface was much less than from the UE1 position. Consequently, the MPCs scattered from the pool were too weak to be identified.

B. NLOS Scenario

The two illustrative example UE positions for typical NLOS environments are circled in Fig. 4(b). UE3 is quite close to the east wing of the SEI building, whereas UE4 is in an open area between two buildings. The spatial power arrivals at the BS for the two UE positions are plotted in Figs. 7 and 8.

Fig. 7(a) shows a cluster with the EoA around 75° and AoA around 105°. If we superimpose this power profile on the photo taken from the BS in Fig. 7(b), we can see that this cluster was from the direction of the UE. Thus, it should be the direct propagation penetrating the SEI building. Compared with the true LOS propagation in Fig. 5(a), the cluster was attenuated and spread considerably. This is expected because of the scattering effect when the waveforms propagated through the walls and windows of the building. The other isolated power arrivals in Fig. 7(a) may be the MPCs reflected from surrounding objects.

The power arrival profile for UE4 is plotted in Fig. 8(a). It can be found that, different from UE3, there are obviously two distinct clusters. The one on the right-hand side has the similar EoA and AoA ranges as that in Fig. 7(a). Therefore, this cluster should be the direct penetrating propagation from the UE. Again, the scattering effect of the walls, windows, and furniture inside the building attenuated and spread the rays. The other cluster with the EoA close to 90° should be the signals that propagated to the rooftops and then diffracted up to the BS. This diffraction can be confirmed in Fig. 8(b), which was over the rooftop of the south wall of the SEI east wing with an LOS path to the BS antenna. Therefore, its incident angle was close to 90° and had an offset to the azimuth/elevation angle of the UE's direction. The same phenomenon was found in [28] for LOS scenario measurements, where such over-rooftop propagation often acted as the secondary strongest path only to the LOS one and therefore was called the *Quasi-LOS* path. From our measurement results in Fig. 8(a), we can see that the *Quasi-LOS* path makes a significant contribution in the received power in such NLOS scenarios. As will be shown in Section VI, the *Quasi-LOS* path plays a critical role in determining the ASA and ESA.

VI. Measurement Results of Angular Power Spread

A. Measurement Results of Power Spectra

As mentioned in Section III-A, 160 channel snapshots were performed at each UE position and 10 most significant MPCs were selected from each snapshot. Thus, from the five UE po-

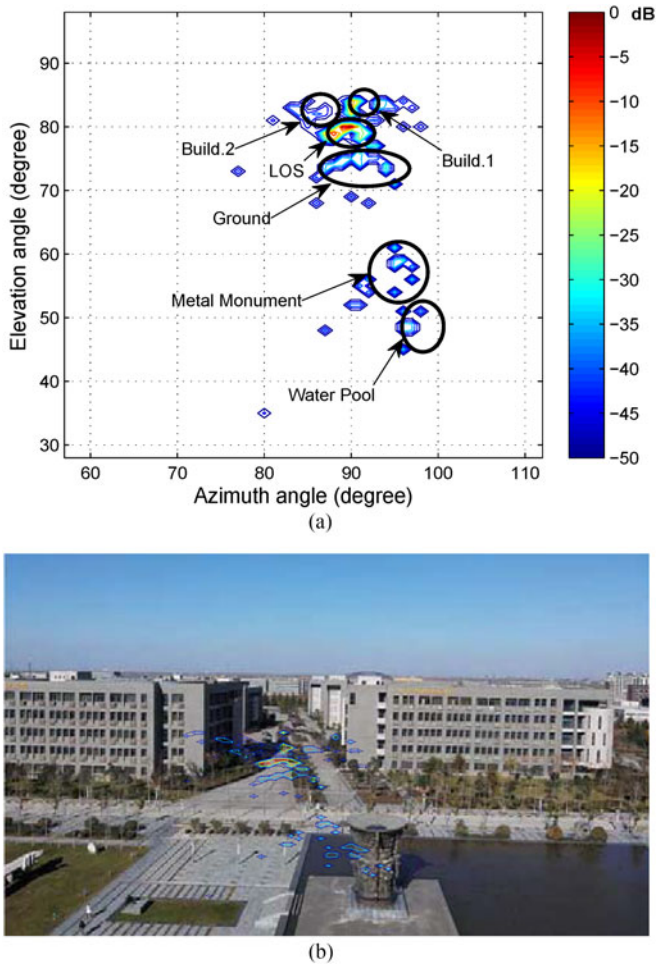

Fig. 5. 2-D angular power profile at the BS for the UE1 position. (a) Azimuth–elevation plane. (b) Estimated power profile in the environment.

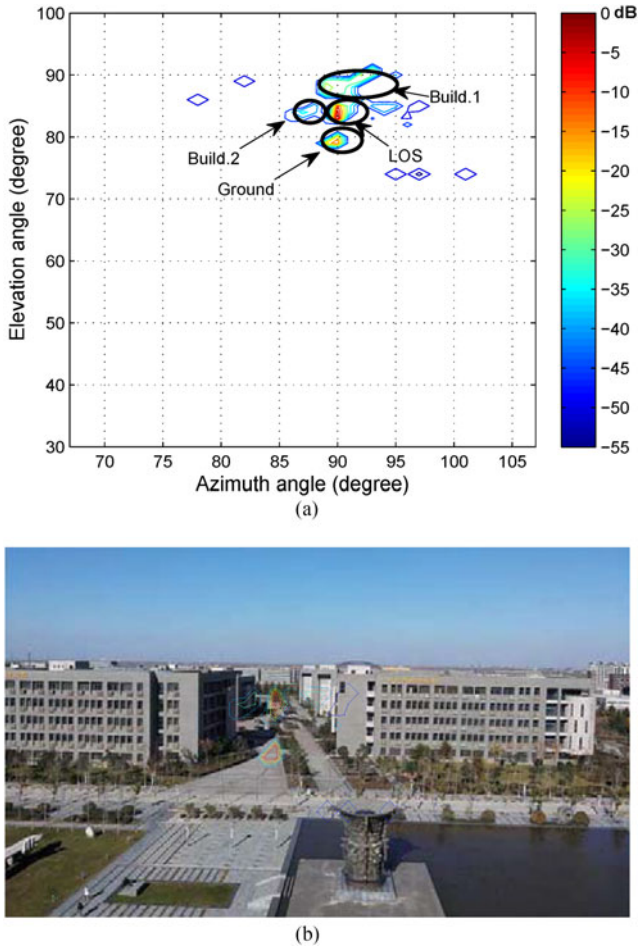

Fig. 6. 2-D angular power profile at the BS for the UE2 position. (a) Azimuth–elevation plane. (b) Estimated power profile in the environment.

sitions at a given transceiver distance, a total of $160 \times 10 \times 5 = 8000$ sample paths were collected. Based on their power and incident angles, the APS and EPS are obtained. As illustrative examples, the APSs and EPSs at the distance of D_2 in the LOS scenario and at D_4 in the NLOS scenario are plotted in Figs. 9 and 10, respectively. This paper mainly focuses on the angular spreads of the power spectra, i.e., ASA and ESA, as given in (2).

As mentioned in Section IV, we have obtained in total 800 snapshots at a given UE–BS distance, and thus the same number of ASA and ESA samples have been collected. The mean and standard deviation (STD) of the samples at each distance in the LOS scenario are plotted in Fig. 11, and the results for NLOS are plotted in Fig. 12. We can see that both curves run in zigzag with the increase of the UE–BS distance. These interesting observations are analyzed in the following sections.

B. ASA and ESA in the LOS Scenario

As shown in Fig. 3(a), the width of the measurement street canyon is actually changing due to the irregular layout of the buildings on both roadsides. Along the position grid of the UE, we can divide the street into four areas according to the roadside building layout, as illustrated in Fig. 3(a). The Area1 and Area3 are *open street* because on both roadsides were gardens, squares, or trees. The Area2 and Area4 are *closed street* because buildings with concrete external walls exist on one or both sides of the street.

It can be seen that the variations of ASA and ESA in Fig. 11 match the change of the street width in Fig. 3(a). Specifically, when the UE was moved in Area1 and Area3, ASA and ESA basically decreased with the increase of the UE–BS distance. When the UE was moved in Area2 and Area4, ASA and ESA increased with the distance. In addition, it can also be seen that the fluctuations of ASA and ESA were identical with each other.

The coincidence of the fluctuation of the measured ASA/ESA and the change of the street width is quite interesting. People may expect a consistent correlation between the angular spreads and the transceiver distance (or the large-scale fading, such as *path loss*), i.e., the angular spreads would vary monotonically with the increase of distance. However, our measurement results have shown that the correlation may not be so straightforward as expected. The phenomena observed may be explained as follows.

We review the definition of angular spreads first. The angular spread is not concerned with the absolute amount of incident

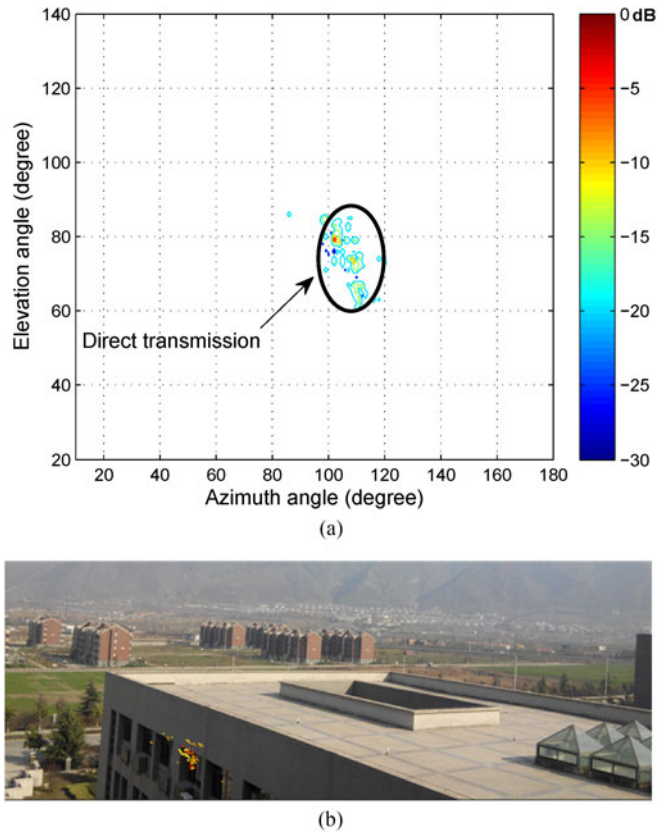

Fig. 7. 2-D angular power profile at the BS for the UE3 position. (a) Azimuth–elevation plane. (b) Estimated power profile in the environment.

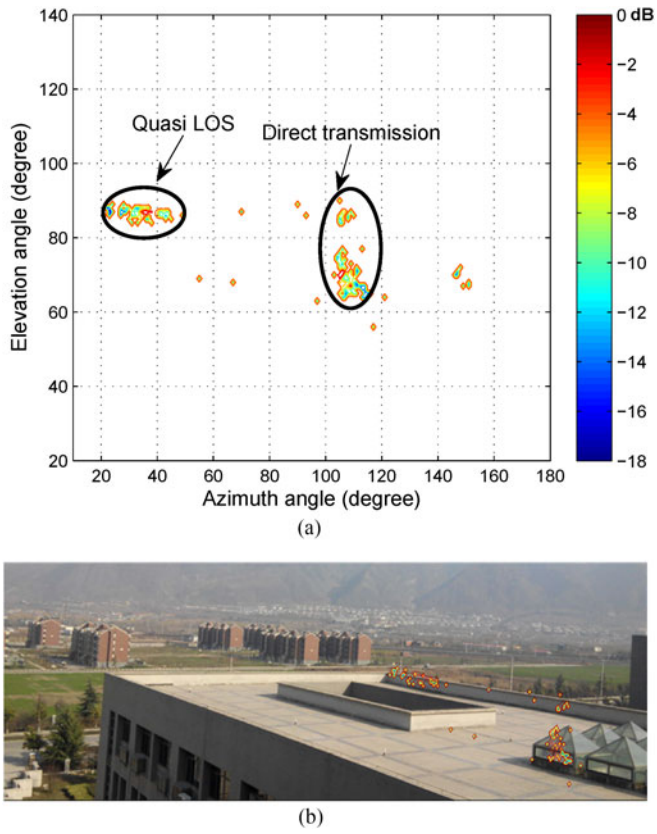

Fig. 8. 2-D angular power profile at the BS for the UE4 position. (a) Azimuth–elevation plane. (b) Estimated power profile in the environment.

power but with the angular distribution. Further, its value depends on the ratio between the arrived power through the most significant MPC (such as the LOS path) and the power through the other *scattered MPCs*[2] that arrive at the receiver in a much wider angular range. If the former is much larger than the latter, the angular spreads should be small. Otherwise, if the scattered MPCs make a considerable contribution in the power spectra, the angular spreads will be large. More importantly, when the UE is moving, the variations of ASA and ESA depend on the portions of the two contributions in the total received power.

The fluctuation of angular spreads in the LOS scenario may be explained as follows.

1) In the closed street (Area1 and Area3), because the buildings were close to the UE, the MPCs reflected from the buildings had relatively high power and thus made considerable contributions in the incident power at the BS. This phenomenon can be observed at the first example UE position, UE1, described in Section V-A. When the UE moved farther away from the BS, the power arrival through the LOS and the reflection paths all decreased due to a larger path loss. However, the power of the MPCs reflected from the surrounding buildings may decrease faster and more significant than the LOS propagation. Consequently, the

[2]For easy presentation, we use the term "scattered MPCs" to generally refer to the nonsignificant propagation paths by reflection and scattering.

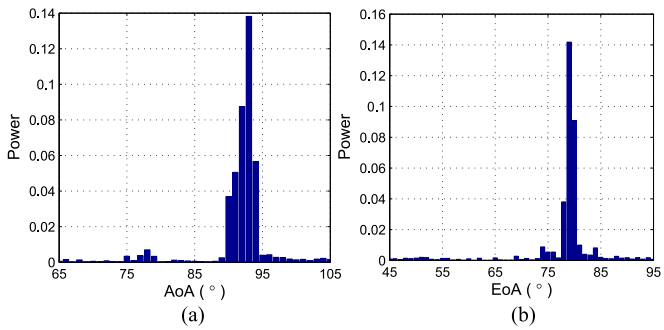

Fig. 9. Measured APS at the distance of D_2 in LOS scenario. (a) Azimuth power spectrum. (b) Elevation power spectrum.

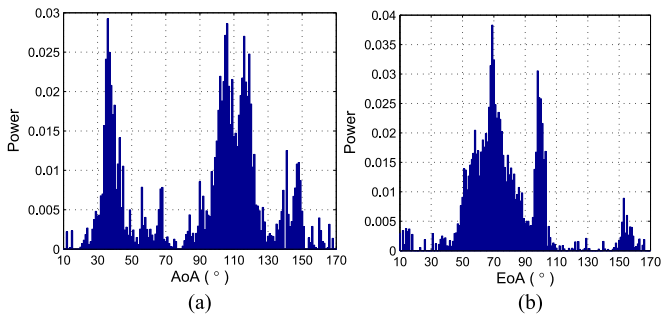

Fig. 10. Measured APS at the distance of D_4 in NLOS scenario. (a) Azimuth power spectrum. (b) Elevation power spectrum.

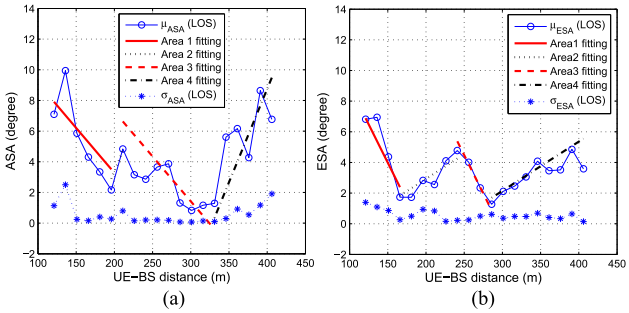

Fig. 11. Mean and STD of the ASA and ESA samples in the LOS scenario. (a) ASA. (b) ESA.

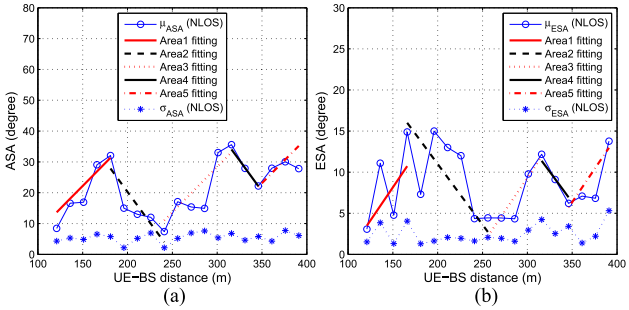

Fig. 12. Mean and STD of the ASA and ESA samples in the NLOS scenario. (a) ASA. (b) ESA.

portion of the power from the scattered MPCs in the total received power decreased, which resulted in the decrease of ASA and ESA.

2) In the open street (Area2 and Area4), the buildings were far away from the UE and hence the MPCs scattered from the buildings were quite weak. This phenomenon can be observed at the example UE position, UE2, described in Section V-A. In this case, the LOS propagation was dominant. When the UE moved further away from the BS, the received power of both the LOS and the scattered MPCs decreased. However, since the latter had already been very small, the decrease of the former was now more significant. Therefore, the portion of LOS power in the total received power decreased and thus ASA and ESA became larger.

The analysis above leads to the following conclusion. In urban street canyon environment with LOS propagation, the channel ASA and ESA at the BS depend on both the UE distance and the street layout. When the street is closed, both angular spreads will decrease with the increase of the UE–BS distance, but they will increase in an open street.

C. ASA and ESA in NLOS Scenario

The results in the NLOS scenario are plotted in Fig. 12. We can see that both curves run in zigzag with the increase of the UE–BS distance. According to the construction layout on the roadsides, the street can be divided into five areas, as illustrated in Fig. 4(a). Area1, Area3, and Area5 are just in front of and quite close to three five-storey buildings, while Area2 and Area4 are open areas in the middle of two buildings.

Again, we can see that the fluctuations of ASA and ESA in Fig. 12 match the street layout. In particular, both angular spreads increased when the UE moved away from the BS in Area1, Area3, and Area5, and decreased in the other two areas. The fluctuations of ASA and ESA were coincident with each other. The NLOS measurement results are analyzed as follows.

1) First, compared with the angular spreads in the LOS scenario, the values in the NLOS scenario were larger. This is expected and the reasons are two fold. On one hand, the direct propagation was spread widely when penetrating the blocking building. On the other hand, as the direct signal was attenuated severely, the scattered MPCs made more significant contributions in the total received power.
2) In Area1, Area3, and Area5, the UE was quite close to the buildings. As shown in the power profile at the example position UE3 in Section V-B, the direct propagation penetrating the building was dominant in the received power. When the UE was moved further away, the direct propagation faded quickly due to the larger path loss and the attenuation by the blocking building. However, the other scattered MPCs, which had already been quite small, may not change too much. Since the portion of the direct power arrival in the total received power decreased, the angular spreads increased.
3) ASA and ESA decreased in Area2 and Area4 where the UE moved away from the BS in the middle of two buildings. As we can see from the power profile at the example position UE4, the over-rooftop diffraction, i.e., the *Quasi-LOS* path, occurred and made the most significant contribution in the total received power. When the UE moved toward south and farther away from the blocking buildings, the direct propagation experienced deeper fading. But the MPCs in the *Quasi-LOS* cluster may not decrease quickly because the over-rooftop diffraction from the UE may be even easier. Since the received power concentrated more on the *Quasi-LOS* path, ASA and ESA decreased quickly.

In summary, in the NLOS scenario in a typical UMa street canyon, the existence of the *Quasi-LOS* path plays a critical role in determining ASA and ESA. Without the *Quasi-LOS* path, both ASA and ESA become larger with the increase of the UE–BS distance because the direct penetrating propagation is attenuated more severely compared with the other scattered MPCs. However, if the *Quasi-LOS* path exists, its power may become more significant when the UE–BS distance increases. Thus, both ASA and ESA will decrease accordingly. Furthermore, a common tendency of ASA and ESA can be observed in these figures. This observation is reasonable, because the azimuth and elevation spreads are originated from the same clusters and hence they should be positively correlated.

VII. Angular Spread Modeling

A. Distribution of ASA and ESA

As presented in Section IV, we collected 800 samples for ASA and ESA at a given UE–BS distance, which are the sample set for curve fitting. Because the transceiver distance and

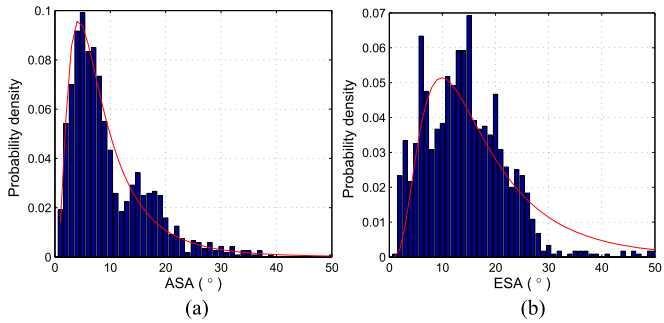

Fig. 13. Distributions of ASA and ESA at D_{17} in the LOS scenario. (Superimposed curves are the best-fitting lognormal pdfs.) (a) Empirical distribution of ASA. (b) Empirical distribution of ESA.

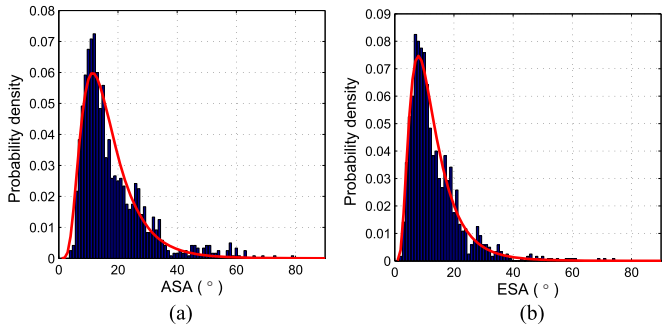

Fig. 14. Distributions of ASA and ESA at D_9 in the NLOS scenario. (Superimposed curves are the best-fitting lognormal pdfs.) (a) Empirical distribution of ASA. (b) Empirical distribution of ESA.

surrounding environment did not change, there was no large-scale fading among these samples and they should be independent identically distributed. For example, the probability histograms of the angular spreads at the distance D_{17} in the LOS scenario and at D_9 in the NLOS scenario are plotted in Figs. 13 and 14, respectively.

We have used the Akaike information criterion (AIC) method to compare the candidate distribution functions, including *chi-square*, *gamma*, *lognormal*, *Poisson*, *Rayleigh*, and *Weibull*, in fitting the probability histograms of ASA and ESA at each distance. In the LOS scenario, the samples at the 20 transceiver distances provide 40 AIC testing results for both ASA and ESA for each distribution pdf. Similarly, in the NLOS scenario, the samples at the 19 transceiver distances provide 38 AIC testing results for each pdf. The averages of the AIC results have shown that the lognormal distribution is the most appropriate in modeling the measurement graphs.

Thus, the distribution of ASA and ESA of the UMa street channels can be expressed as

$$f_s(x) = \frac{1}{\sqrt{2\pi}\sigma_s} e^{-\frac{(\ln x - \mu_s)^2}{2\sigma_s^2}} \tag{6}$$

where μ_s and σ_s are the mean and STD of the lognormal pdf. The best-fitting functions are determined by matching the measured probability histograms using the least squares errors. Then, the key issue is to determine the model parameters for both angular spreads in specific environments.

TABLE I
LINEAR REGRESSION COEFFICIENTS FOR EACH AREA

Scenario		Range (m)	A_{ASA}	B_{ASA}	A_{ESA}	B_{ESA}
LOS	Area1	121–181	−0.08	19.35	−0.12	22.04
	Area3	241–301	−0.03	10.55	−0.08	24.50
	Area2	181–241	0.18	−32.7	0.04	−5.61
	Area4	301–406	0.07	−18.8	0.02	−4.54
NLOS	Area1	67–91	0.39	−39.5	0.19	−19.4
	Area3	129–183	0.36	−79.4	0.14	−32.7
	Area5	206–230	0.13	−19.6	0.15	−46.7
	Area2	91–129	−0.35	89.6	−0.10	30.4
	Area4	183–206	−0.44	176.7	−0.19	75.1

TABLE II
FUNCTION COEFFICIENTS OF THE MEAN AND STD OF THE LOGNORMAL MODEL

Scenario	A_{ASA}	B_{ASA}	A_{ESA}	B_{ESA}	σ^*_{AE}
Closed Street	−0.055	14.95	−0.10	23.27	$U[0-2]^\circ$
Open Street	0.25	−25.75	0.03	−5.08	
Without Quasi-LOS	0.29	−46.17	0.16	−32.93	$U[2-7]^\circ$
With Quasi-LOS	−0.40	133.15	−0.15	52.75	

σ^*_{AE} : the values listed below are applicable to both ASA and ESA.

B. Lognormal Model Parameter Determination

In this section, the functions for the mean and STD of the lognormal model are established with respect to the UE–BS distance and environments based on our measurement results. Inspired by the zigzag curves in Figs. 11 and 12, we adopt linear functions for the mean of ASA and ESA in each area in the two scenarios. The mean of the lognormal model can be approximated by

$$\mu_s = A \cdot d + B \tag{7}$$

where d is the UE–BS distance, A and B are the coefficients that depend on the area (environment) and are determined by linear regression to the measurement results.

The obtained model coefficients are listed in Table I. For easy comparison, the areas where ASA/ESA have the same variation tendency are listed together in Table I.

As we can see, in the LOS scenario, the slopes of the linear functions for the means of ASA and ESA in Area1 and Area3 are both negative, while those in Area2 and Area4 are both positive. For the NLOS scenario, the slopes of the linear functions for the means of ASA and ESA in Area1, Area3, and Area5 are all positive, and those in Area2 and Area4 are negative. This observation suggests that we can simplify the functions by combining the areas where ASA and ESA have the same variation tendency. Thus, we define four propagation cases: *open LOS street*, *closed LOS street*, *NLOS street without "Quasi-LOS,"* and *NLOS street with "Quasi-LOS."* The average of the linear function coefficients are used as the final parameters for the four cases, which are listed in Table II. The linear regression curves are plotted in Figs. 11 and 12, where we can see a good match between the model and the measurement results.

The STD of ASA and ESA distributions σ_s at different distances are also plotted in Figs. 11 and 12. As observed, the dependence of the STD on the UE distance and the street layout is not clear. Instead, the STD samples vary slightly and randomly within the range of about $[0-2]^\circ$ and $[2-7]^\circ$ in the LOS and NLOS scenarios, respectively. Therefore, we propose to model σ_s by uniform distributions inside the corresponding ranges for either scenario.

C. Angular Spread Value Generation for Channel Realization

The model defined by (6) and (7) can be used to generate the angular spreads for FD-MIMO system simulations in a UMa street canyon environment. The ASA and ESA samples are randomly generated by the following steps.

1) According to the target application environment, select the specific propagation case listed in Table II.
2) Calculate the means of the lognormal distributions for ASA and ESA, denoted by $\mu_{s,a}$ and $\mu_{s,e}$, respectively, using the linear function in (7) and the coefficients obtained from Table II.
3) Generate the STDs of the lognormal distributions for ASA and ESA, denoted by $\sigma_{s,a}$ and $\sigma_{s,e}$, respectively, by uniformly selecting two numbers in the ranges given in Table II.
4) Generate two random numbers according to the lognormal distribution with the means and STDs determined in steps 2) and 3) for ASA and ESA.

VIII. Cross Correlation Between Angular Spreads and DS

The correlations among the large-scale channel parameters are referred to as the *cross correlations*. In this section, the DS measured at different UE–BS distances in this campaign is first presented and then the cross-correlation coefficients among the space- and time-domain parameters, ASA, ESA, and DS, are evaluated.

A. DS Variation Along the Rx Position Grids

Similar to the analysis of angular spreads, we can get a sample of DS from a channel snapshot. The averages of the DS samples at the UE–BS distances in the LOS and NLOS scenarios are plotted in Fig. 15. As we can see, both curves run in zigzag with the increase of the UE–BS distance. Moreover, similar to the angular spreads, the fluctuation of DS in the LOS and NLOS scenarios also matches the change of the street layouts in Figs. 3 and 4. It can also be observed that the variation tendency of DS is similar to those of ASA and ESA, as plotted in Figs. 11 and 12.

B. Cross-Correlation Analysis

The cross-correlation coefficients among ASA, ESA, and DS are calculated as follows. At first, they are regarded as random variables (RVs) and denoted by X_{DS}, X_{ASA}, and X_{ESA}. In the LOS scenario, the average values of ASA, ESA, and DS samples at the UE–BS distances from D_1 to D_{20}, as plotted in Figs. 11(a), 11(b), and 15(a), are the observation sequences of

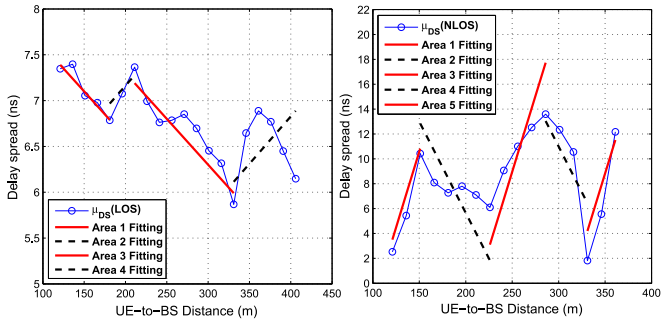

Fig. 15. Mean value of the DS samples in the LOS and NLOS scenarios. (a) LOS scenario. (b) NLOS scenario.

TABLE III
Cross-Correlation Coefficients

Scenario	ASA versus ESA	ASA versus DS	ESA versus DS
LOS	0.71	0.39	0.35
NLOS	0.32	0.27	−0.086

the three RVs. Then the cross-correlation coefficient between DS and ASA is calculated by

$$\rho = \frac{\mathrm{cov}\left(X_{\mathrm{DS}}, X_{\mathrm{ASA}}\right)}{\sqrt{\mathrm{var}\left(X_{\mathrm{DS}}\right)\mathrm{var}\left(X_{\mathrm{ASA}}\right)}} \tag{8}$$

where $\mathrm{cov}(\cdot)$ and $\mathrm{var}(\cdot)$ are the covariance and variance of the given sequence(s), respectively. The correlation coefficients between DS and ESA and between ASA and ESA are calculated in the same way. Similarly, for the NLOS scenario, the measured average ASA, ESA, and DS values at the UE–BS distances from D_1 to D_{19} are the observation sequences of the three RVs, as plotted in Figs. 12(a), 12(b), and 15(b). Then the cross-correlation coefficients are calculated by (8).

The results are listed in Table III. As expected, ASA, ESA, and DS are positive correlated in most scenarios. Moreover, it is confirmed that they are more correlated in the LOS scenario than in the NLOS scenario.

The results obtained in this work can be used to adjust the parameters specified in the 3-D channel models.

IX. Discussion on the Measurement Conditions and Future Works

The full 3-D channel modeling should include description of the ray departure and arrival directions (bidirectional) in both the azimuth and elevation domains (3D) and with cross polarizations (dual polarimetric) [14], [15]. The measurement campaign in this work focuses on the dynamics and variation of the large-scale spatial parameters, ASA and ESA, along urban streets. The limits of the measurements in this work are discussed as follows.

A. Single Polarization

In this paper, the transceivers utilized linearly copolarized dipoles and the measurement and modeling were based on the

signals in +45° polarization. Due to the depolarization effect of the wireless channels, the received signals will have components in the cross polarizations. Capturing and analyzing the signals using only a single dipole in one polarization actually loses the cross-polarized component. As mentioned in Section III-A, when one Tx dipole was transmitting, all of the 32 dipoles in the Rx UPA captured the sounding signals, including 16 copolarized and 16 cross-polarized dipoles. It was observed that the power on the latter was much smaller than that on the former. Thus, the majority of the received power was still in the copolarized component and captured, which was used to calculate the angular spreads.

Most stochastic SCMs employ a complex polarimetric path weight matrix providing the attenuation according to the polarization (i.e., VV, VH, HV, and HH where "V" and "H" mean vertical and horizontal polarizations, respectively). Since we utilized the copolarized transceiver antennas, the items "VV" and "HH" in the matrix were measured in this work. Therefore, the dynamics of the angular spreads are evaluated for the copolarized path attenuation.

To characterize the full power of a path, we need to consider both polarizations, which can be done by combining the complex responses on the $\pm 45^\circ$ polarized dipoles. This is an interesting topic for further research.

B. Data Model

As proposed in [29], a complete data model should include the specular components and statistically distributed dense multipath components. In this work, we focus on the large-scale variation of the angular and delay spreads. These parameters are mainly determined by the significant/dominant MPCs. Therefore, a simplified channel model is adopted as given in (1). For the purpose to calculate the spreads, the ten most significant MPCs were selected. It has been observed that the power of the other MPCs was smaller than 20 dB attenuation of the most significant component.

C. Cyclic Behavior of the Azimuth Power Spectrum

Since a UE is usually surrounded by buildings, trees, and other objects, there exist paths from the opposite side of the UE's antenna that may be reflected to the BS. Therefore, it would be better to utilize an uniform circular array at the UE side [15]. Due to the directionality of a UPA, the MPCs from the back of the UPA were not measured. Nevertheless, because these paths need to travel longer distances than those departing from the front side of the Tx, their power is generally much smaller due to the path loss. Since the angular spreads studied in this paper are mainly determined by the most significant paths, the MPCs from the back of the Tx should not affect the results significantly.

D. Site-Specific Measurement and Model Generalization

In this work, two representative streets were selected for the LOS and NLOS UMa street scenarios. The interesting behaviors of the variations of ASA and ESA were observed in these two streets. The measurement results provide new insight into the urban street propagation characteristics. The channel properties should be related to the street orientation, roadside buildings, and locations of the transceivers. Thus, to apply the models obtained in this work, the street environment should be similar to the streets in this campaign. To generalize the street channel model, more field measurement data are needed to further verify and refine the findings in this paper.

X. Conclusion

In this paper, we present a field measurement campaign on the 3-D UMa street channels. An MIMO sounder with two UPAs has been used to measure the temporal and spatial power arrival profiles of the MPCs at the BS. The match between the fluctuations of ASA, ESA, and DS and the change of the street environment reveals insightful observations on the channel propagation mechanisms. In the LOS scenario, the street environment can be categorized into "closed street" and "open street." Both ASA and ESA decrease with the increase of UE–BS distance in the former case, but the tendency is reversed in the latter. The NLOS scenario also includes two cases depending on the existence of the *Quasi-LOS* path, which is caused by the over-rooftop diffraction. The correlations between the angular spreads and UE–BS distance in the two cases are also opposite. The underlying propagation mechanisms are investigated by analyzing the 2-D spatial power profiles from typical UE positions in the four cases. We have also proposed to use the lognormal distributions to model ASA and ESA in UMa street canyon environments and have defined the linear functions to calculate the pdf parameters. Finally, the cross-correlation coefficients among the large-scale parameters of ASA, ESA, and DS are evaluated. The results presented in this paper shed light on the 3-D propagations in typical UMa street channels and can help to extend the current SCMs. Properly characterzing the 3-D propagations requires intensive field measurement and modeling works. For example, the azimuth- and elevation-related parameters in different polarizations are subject to further confirmation. The cross correlations among the large-scale parameters, such as path loss and angular spreads, need to be studied. To evaluate and optimize FD-MIMO and other emerging technologies for dense networks [30] based on the 3-D SCMs are also interesting research issues.

References

[1] Y.-H. Nam *et al.*, "Full-dimension MIMO (FD-MIMO) for next generation cellular technology," *IEEE Commun. Mag.*, vol. 51, no. 6, pp. 172–179, Jun. 2013.

[2] "Spatial channel model for multiple input multiple output (MIMO) simulations (Release 7)," 3GPP Technical Specification Group Radio Access Networks, Tech. Rep. TR 25.996, v7.0.0, Jun. 2007.

[3] "WINNER II channel models," Wireless World Initiative New Radio Project, Tech. Rep. IST-4-027756, D.1.1.2 V1.2, Sep. 2007.

[4] "D5.3: WINNER+ final channel models," Wireless World Initiative New Radio Project, Tech. Rep. V1.0, Jun. 2010.

[5] R. Verdone and A. Zanella *et al.*, *Pervasive Mobile and Ambient Wireless Communications COST Action 2100*. Berlin, Germany: Springer-Verlag, 2012.

[6] "Study on 3D channel model for LTE (Release 12)," 3GPP Technical Specification Group Radio Access Networks, Tech. Rep. TR 36.873 V12.2.0, Jun. 2015.

[7] "Study on 3D-channel model for elevation beamforming and FD-MIMO studies for LTE," 3GPP TSG RAN Plenary, Barcelona, Spain, Study Item Description RP-122034, Dec. 2012.
[8] K. Kalliola, K. Sulonen, H. Laitinen, O. Kivekas, J. Krogerus, and P. Vainikainen, "Angular power distribution and mean effective gain of mobile antenna in different propagation environments," *IEEE Trans. Veh. Technol.*, vol. 51, no. 5, pp. 823–838, Sep. 2002.
[9] N. Blaunstein *et al.*, "Signal power distribution in the azimuth, elevation and time delay domains in urban environments for various elevations of base station antenna," *IEEE Trans. Antennas Propag.*, vol. 54, no. 10, pp. 2902–2916, Oct. 2006.
[10] J. Medbo, H. Asplund, J.-E. Berg, and N. Jalden, "Directional channel characteristics in elevation and azimuth at an urban macrocell base station," in *6th Eur. Conf. Antennas Propag.*, Prague, Czech Republic, Mar. 2012, pp. 428–342.
[11] F. Pei, J. Zhang, and C. Pan, "Elevation angle characteristics of urban wireless propagation environment at 3.5 GHz," in *IEEE 78th Veh. Technol. Conf. (VTC Fall)*, Las Vegas, NV, USA, Sep. 2013, pp. 1–5.
[12] T. Thomas, F. Vook, E. Visotsky, E. Mellios, G. Hilton, and A. Nix, "3D extension of the 3GPP/ITU channel model," in *IEEE 77th Veh. Technol. Conf. (VTC Spring)*, Dresden, Germany, Jun. 2013, pp. 1–5.
[13] F. Fuschini, H. El-Sallabi, V. Degli-Esposti, L. Vuokko, D. Guiducci, and P. Vainikainen, "Analysis of multipath propagation in urban environment through multidimensional measurements and advanced ray tracing simulation," *IEEE Trans. Antennas Propag.*, vol. 56, no. 3, pp. 848–857, Mar. 2008.
[14] G. Sommerkorn, M. Kaske, C. Schneider, S. Hafner, and R. Thoma, "Full 3D MIMO channel sounding and characterization in an urban macro cell," in *31st URSI Gen. Assem. Sci. Symp.*, Beijing, China, Aug. 2014, pp. 1–4.
[15] M. Narandzic, C. Schneider, M. Kaske, and S. Jackel, "Large-scale parameters of wideband MIMO channel in urban multi-cell scenario," in *5th Eur. Conf. Antennas Propagation*, Rome, Italy, Apr. 2011, pp. 3759–3763.
[16] M. Narandzic, C. Schneider, W. Kotterman, and R. S. Thoma, "Quantification of scenario distance within generic WINNER channel model," *Int. J. Antennas Propag*, vol. 2013, no. 2, pp. 188–192, Feb. 2013.
[17] M. Narandzic, M. Kaske, G. Sommerkorn, S. Jackel, C. Schneider, and R. Thoma, "Variation of estimated large-scale MIMO channel properties between repeated measurements," in *IEEE 73rd Veh. Technol. Conf. (VTC Spring)*, Budapest, Hungary, May. 2011, pp. 1–5.
[18] M. Narandzic *et al.*, "3D-antenna array model for IST-WINNER channel simulations," in *IEEE 65th Veh. Technol. Conf. (VTC Spring)*, Dublin, Ireland, Apr. 2007, pp. 319–323.
[19] Y. Yu, J. Zhang, M. Shafi, and P. A. Dmochowski, "Measurements of 3D channel impulse response for outdoor-to-indoor scenario: Capacity predictions for different antenna arrays," in *IEEE 26th Annu. Int. Symp. Pers., Indoor, Mobile Radio Commun.*, Hong Kong, Sep. 2015, pp. 408–413.
[20] D. Du, J. Zhang, C. Pan, and C. Zhang, "Cluster characteristics of wideband 3D MIMO channels in outdoor-to-indoor scenario at 3.5 GHz," in *IEEE 79th Veh. Technol. Conf. (VTC Spring)*, Seoul, South Korea, May. 2014, pp. 1–6.
[21] Q. Luo, F. Pei, J. Zhang, and M. Zhang, "3D MIMO channel model based on field measurement campaign for UMa scenario," in *IEEE Wireless Commun. Netw. Conf.*, Istanbul, Turkey, Apr. 2014, pp. 171–176.
[22] Z. Zhong, X. Yin, X. Li, and X. Li, "Extension of ITU IMT-advanced channel models for elevation domains and line-of-sight scenarios," in *IEEE 78th Veh. Technol. Conf. (VTC Fall)*, Las Vegas, NV, USA, Sep. 2013, pp. 1–5.
[23] R. Zhang, L. Cai, X. Lu, P. Yang, and J. Zhou, "Elevation domain measurement and modeling of UMa uplink channel with UE on different floors," in *IEEE Int. Conf. Comput., Netw. Commun.*, Anaheim, CA, USA, Feb. 2015, pp. 679–684.
[24] R. Zhang, X. Lu, W. Duan, L. Cai, and J. Wang, "Elevation domain channel measurement and modeling for FD-MIMO with different UE height," in *IEEE Wireless Commun. Netw. Conf.*, New Orleans, LA, USA, Mar. 2015, pp. 70–75.
[25] Y. Zhang, R. Zhang, S. X. Lu, W. Duan, and L. Cai, "Measurement and modeling of indoor channels in elevation domain for 3D MIMO applications," in *IEEE Int. Conf. Commun. Workshop Small Cell 5G Netw.*, Sydney, NSW, Australia, Jun. 2014, pp. 659–664.
[26] J. Wang, R. Zhang, W. Duan, S. X. Lu, and L. Cai, "Angular spread measurement and modeling for 3D MIMO in urban macrocellular radio channels," in *IEEE Int. Conf. Commun. Workshop 5G Technol.*, Sydney, NSW, Australia, Jun. 2014, pp. 20–25.
[27] R. Zhang, S. Wang, X. Lu, W. Duan, and L. Cai, "Two-dimensional DoA estimation for multipath propagation characterization using the array response of PN-sequences," *IEEE Trans. Wireless Commun.*, vol. 15, no. 1, pp. 341–356, Jan. 2016.
[28] K. Kalliola, H. Laitinen, P. Vainikainen, M. Toeltsch, J. Laurila, and E. Bonek, "3-D double-directional radio channel characterization for urban macrocellular applications," *IEEE Trans. Antennas Propag.*, vol. 51, no. 11, pp. 3122–3133, Nov. 2003.
[29] M. Landmann, M. Kaske, and R. S. Thoma, "Impact of incomplete and inaccurate data models on high resolution parameter estimation in multidimensional channel sounding," *IEEE Trans. Antennas Propag.*, vol. 60, no. 2, pp. 557–573, Feb. 2012.
[30] R. Yao, Y. Liu, L. Lu, G. Y. Li, and A. Maaref, "Cooperative precoding for cognitive transmission in two-tier networks," *IEEE Trans. Commun.*, vol. 64, no. 4, pp. 1423–1436, Apr. 2016.

Ruonan Zhang (S'09–M'10) received the B.S. and M.Sc. degrees from Xi'an Jiaotong University, Xi'an, China, in 2000 and 2003, respectively, and the Ph.D. degree from the University of Victoria, Victoria, BC, Canada, in 2010, all in electrical and electronics engineering.

He worked as an IC Architecture Engineer with Motorola Inc. and Freescale Semiconductor Inc., Tianjin, China, from 2003 to 2006. Since 2010, he has been with the Department of Communications Engineering, Northwestern Polytechnical University, Xi'an, China, where he is currently a Professor. His research interests include wireless channel measurement and modeling, architecture and protocol design of wireless networks, and satellite communications.

Dr. Zhang received the New Century Excellent Talent Grant from the Ministry of Education of China, and the Best Paper Award at the IEEE Conference on Networking and Network Applications 2016. He has served as a Local Arrangement Cochair for the IEEE International Conference on Communications in China 2013, and as an Associate Editor of the *Journal of Communications and Networks*.

Xiaofeng (Stan) Lu (M'11) received the B.Sc. degree from University of Electronic Science and Technology of China, the M.Sc. degree from Lanzhou University, and the Ph.D. degree from Xi'an Jiaotong University, all in electrical and electronics engineering.

He is currently an Algorithm Engineer with the Huawei Technologies Ltd., Shanghai, China. His research interests include digital wireless communications, wireless channel measurement and modeling, distributed space-time coding, cooperative communications, and multiple-input–multiple-output systems.

Jianping Zhao received the B.S. degree in physics and the M.S. degree in signal and information processing from Xidian University, Xi'an, China, in 1991 and 1996, respectively, and the Ph.D. degree in signal and information processing from Beijing University of Posts and Telecommunications, Beijing, China, in 1999.

He is currently a Principle Engineer with Huawei Technologies Ltd., Shanghai, China, in the area of wireless communications. His research interests include wireless channel modeling, antenna and RF innovation, and antenna system prototyping.

Lin Cai (S'00–M'06–SM'10) received the M.A.Sc. and Ph.D. degrees in electrical and computer engineering from the University of Waterloo, Waterloo, ON, Canada, in 2002 and 2005, respectively.

Since 2005, she has been with the Department of Electrical & Computer Engineering, University of Victoria, Victoria, BC, Canada, where she is currently a Professor. Her research interests include several areas in communications and networking, with a focus on network protocol and architecture design supporting emerging multimedia traffic over wireless, mobile, ad hoc, and sensor networks.

Dr. Cai has received the NSERC Discovery Accelerator Supplement Grant in 2010 and 2015, respectively, and the best paper awards of the IEEE International Conference on Communications 2008 and the IEEE Wireless Communications and Networking Conference 2011. She has served as a Technical Program Committee symposium Cochair for the IEEE Global Communications Conference (GLOBECOM)'10 and GLOBECOM'13, and the Associate Editor of the IEEE TRANSACTIONS ON WIRELESS COMMUNICATIONS, the IEEE TRANSACTIONS ON VEHICULAR TECHNOLOGY, the EURASIP *Journal on Wireless Communications and Networking*, the *International Journal of Sensor Networks*, and the *Journal of Communications and Networks*.

Jiao Wang received the B.S. degree from Zhengzhou University of Aeronautics, Zhengzhou, China, in 2012, and the M.Sc. degree from Northwestern Polytechnical University, Xi'an, China, in 2015, all in electrical and electronics engineering.

Her research interests include wireless channel measurement and modeling, MIMO technologies, and array signal processing.